RSC Advances

PAPER

View Article Online
View Journal | View Issue

Cite this: *RSC Adv.*, 2024, **14**, 39498

Unveiling a growth temperature-dependent ultra-sensitive tetragonal scheelite $BiVO_4$ thin film-based gas sensor for ammonia volatilization at room temperature†

Santhosh Nallakumar,[a] Logu Thirumalaisamy,[b] Sivaperuman Kalainathan,[c] Vijaya B,[a] Anand Sekar[a] and Muthurakku Usha Rani *[a]

Received 17th November 2024
Accepted 23rd November 2024

DOI: 10.1039/d4ra08169b

rsc.li/rsc-advances

Ammonia (NH_3) vapour is considered as a hazardous volatile, which has the potential to cause health concerns in humans. Exposure to NH_3 can lead to potentially fatal, severe burn injuries to human eyes, can cause encephalopathy, and also affects various physiological systems, including the liver, the kidneys and the immune system. Due to these prime factors, the advancement of chemi-resistive ammonia gas sensors at room temperature has drawn considerable attention among researchers. In this current work, tetragonal scheelite (T_s)-$BiVO_4$ thin films were deposited by varying the substrate (growth) temperature *via* the chemical spray pyrolysis method. The deposited thin films were subjected to structural, optical, morphological and gas sensing assessment. The gas sensing results indicate that the BV250 film has an ultra-high sensor response (I_{gas}/I_{air} = 900 for 75 ppm) towards ammonia vapour at room temperature. The pro-longevity of the sensor is outstanding (I_{gas}/I_{air} = 58.2 for 25 ppm) even after 50 days at room temperature. Furthermore, it demonstrates excellent selectivity, rapid response time (190 ± 4 s)/recovery time (16 ± 5 s) and repeatability (up to 4 cycles), and performs well in relatively humid conditions. This study offers insights into T_s-$BiVO_4$ thin films as a sensing layer in a chemi-resistive gas sensor for ammonia detection at room temperature.

Introduction

Environmental air quality is getting worse day by day, which can lead to severe metabolic effects on the human body.[1–6] There exists a significant need for an E-nose, which can detect toxic gases with ultra-high sensing performance and low cost. Gas sensors play vital roles in various fields, such as air quality monitoring, fertilizer production, the automotive industry, and the pharmaceutical industry, to identify flammable and hazardous gas leakages.[1,3,6] Amongst the various hazardous gases, ammonia (NH_3) is a reducing toxic gas that poses a significant threat to the mucous membranes in the human respiratory system, skin and eyes.[7,8] Prolonged inhalation over a short span will lead to severe lung swelling and sometimes even death (the OSHA limit for NH_3 is 25 ppm over 8 hours).[2,7] Thus far, commercially available ammonia gas sensors are bulk or semiconducting materials that require thermal energy (200–450 °C) assistance for gas detection. This leads to high power consumption and also restricts their manufacturing in wearable electronic devices. Consequently, there is a growing demand for room temperature-operated ultra-sensitive ammonia gas sensors that can be used across various domains, such as in medical, industrial, agricultural, living environment, and military applications.[5]

To enhance the sensing performance of NH_3 sensors at low operating temperatures (room temperature), researchers have explored different materials as sensing layers.[9,10] For over a decade, metal oxide semiconductors (MOS's) have been given enormous consideration in various applications, such as gas sensors, solar cells, batteries, *etc.*.[3,8,11] MOS-based NH_3 gas sensors have been developed due to their excellent sensitivity, durable stability, compatibility and cost-effectiveness. Nevertheless, the high operating temperature requirement of NH_3 gas sensors limits their realm of applicability.[6,12,13] Ternary metal oxides are promising candidates as a sensing layer rather than binary metal oxides due to their versatile features, like high sensor response, rapid response and recovery times, and prolonged stability.[14–16] In recent years, bismuth-based metal oxide semiconductors have received extensive attention in photocatalytic water splitting, gas sensors, *etc.*.[17,18] $BiVO_4$ thin films are classified as n-type semiconductors and their band gap energy

[a]*Department of Physics, School of Advanced Sciences, VIT, Vellore, 632014, India. E-mail: usharani.m@vit.ac.in*

[b]*Department of Physics, G.T.N Arts College (Affiliated to Madurai Kamaraj University), Dindigul, India*

[c]*Centre for Nanotechnology Research, VIT, Vellore, 632014, India*

† Electronic supplementary information (ESI) available. See DOI: https://doi.org/10.1039/d4ra08169b

lies between 2.4 and 2.9 eV, which makes them a suitable choice for adsorbed oxygen molecules to entrapping the electron on the surface. $BiVO_4$ exists as three polymorphs, namely monoclinic scheelite – $BiVO_4$ (M_s), tetragonal scheelite – $BiVO_4$ (T_s), and tetragonal zircon – $BiVO_4$ (T_z).[19–21] Among these polymorphs, M_s-$BiVO_4$ has been extensively reported due to its lower bandgap energy, and its band assignment showed favourability in gas sensor, photocatalytic and other applications. Subsequently, T_s-$BiVO_4$ polymorphs have also exhibited moderate potential in photocatalytic applications. In contrast, the T_z-$BiVO_4$ polymorph exhibits the lowest photocatalytic activity, which is attributed to its wide bandgap energy (2.9 eV). Thus far, a literature survey shows that many researchers have explored M_s-$BiVO_4$ and T_z-$BiVO_4$ polymorphism for gas sensors, photocatalysts and other applications.[20,22,23]

A comparative literature survey indicates that thus far, no reports are available on T_s-$BiVO_4$ polymorphs in gas sensing applications. Due to its desirable bandgap energy and physicochemical properties, tetragonal scheelite-$BiVO_4$ (T_s-$BiVO_4$) thin films are also a promising choice for sensor applications, as they can enhance the sensor response. This present study explores the physicochemical attributes of T_s-$BiVO_4$ thin film by varying the growth temperature through the chemical spray pyrolysis technique. Furthermore, T_s-$BiVO_4$ thin films are subjected to a selectivity test with various volatile organic liquids at room temperature. Our findings reveal that BV250 (T_s-$BiVO_4$) thin films are highly selective towards ammonia detection within the OSHA exposure limit. Further insights are discussed below in this research article.

Experimental

$BiVO_4$ thin film deposition

To prepare the $BiVO_4$ thin films, $Bi(No_3)_3 \cdot 5H_2O$ and NH_4VO_3 were utilized as precursor chemicals. The metal precursor was dissolved using a solvent mixture of nitric acid and deionized water (in a ratio of 1200 μL : 15 mL). Then, 0.9701 g of $Bi(No_3)_3 \cdot 5H_2O$ and 0.2339 g of NH_4VO_3 were dissolved into two separate 15 mL precursor solvents and stirred continuously for 30 min. Subsequently, a transparent vanadium solution was added to the bismuth solution and stirred for an additional 15 min, before spraying. During spray pyrolysis, certain parameters were maintained as constant, namely spray angle (42°), nozzle-to-substrate distance (30 cm), hot plate temperature (150, 200, 250 °C), spray time (10 s) and interval (2 min).

Characterization and sensor fabrication

A powder X-ray diffractometer was used to obtain the diffraction pattern of the spray-deposited film, which paved the way for the crystal structure and phase purity to be confirmed using a D8 – Advanced Bruker instrument. The structural conformation and vibrational modes of the deposited thin films were assessed through Raman spectroscopy, using a Horiba XploRA™ (100–1200 nm and 532 nm). Absorbance spectra were used to acquire the optical properties of the thin films, and were evaluated *via* a Cary UV-vis-NIR Spectrometer within the range of 20–2500 nm. Topographical 2D and 3D images and surface roughness-related profiles were estimated using atomic force microscopy *via* a Nanosurf Easyscan. Ossila contact angle (V3.0) measurement was carried out to identify the moisture-resisting capability of the deposited films. The gas sensing analysis was carried out using a home-made gas sensing setup, depicted in Fig. 1. A thin film sensor of dimensions 1.5 × 1.5 cm was used for the gas sensing analysis, and on the top of the sensor surface, silver conducting paste was used to create an ohmic contact with the help of low-resistance copper wire. Then, the fabricated thin film sensor was placed inside the gas sensing chamber and connected to a Keithley electrometer (6517B). Initially, ambient air was allowed into the gas sensing chamber to obtain a stable baseline current (I_{air}). Volatile organic liquids concentration were calculated using the static gas distribution

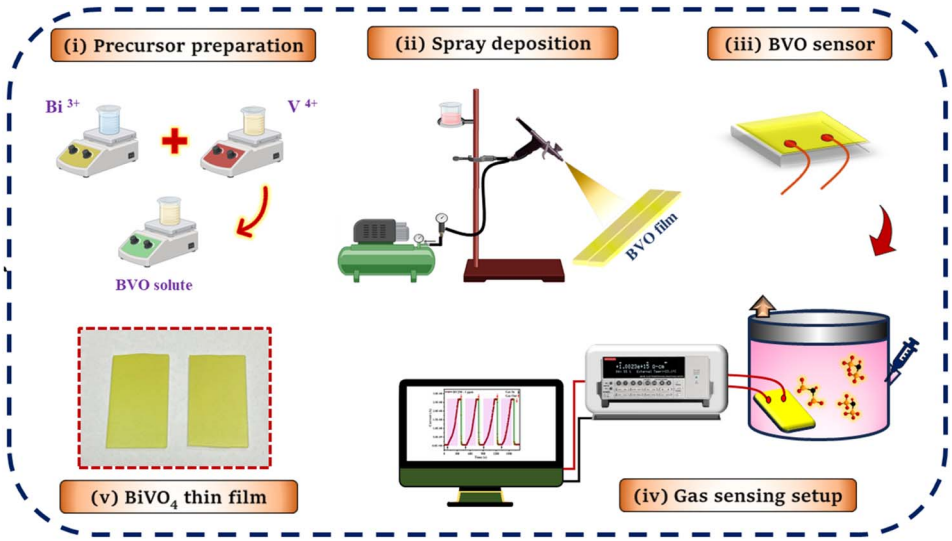

Fig. 1 Schematic diagram of the preparation, deposition and gas sensing measurements of the $BiVO_4$ thin films.

method and then purged into the gas-sensing chamber's inlet. As a consequence of VOC purging, changes in the baseline current were observed. Then, the system was allowed to reach a stable value (I_{gas}). Finally, the residuals were released using the outlet value. All of the necessary gas-sensing analyses were carried out at room temperature.

Results and discussion

Film thickness measurement

The substrate temperature dependence of the $BiVO_4$ thin film thickness can be determined by creating a step on the coated surface and then using a surface profilometer (DektakXT – Bruker) at different points ($n = 2$). This method is accurate and reliable, and it can be used for a wide range of thin film materials. This study investigates the correlation between the thickness of the film and its gas sensing performance towards the target gas (ammonia). As the substrate temperature increases, the film thickness also rises. The substrate temperature-dependent $BiVO_4$ thin film thickness was found to be 695 ± 0.021 nm, 765 ± 0.007 nm, and 895 ± 0.007 nm for the BV150, BV200 and BV250 thin films, respectively. Hence, the substrate temperature affects the decomposition rate of the precursor and the rate of film growth, which quickly influences the thickness of the film.[24–26] This favours the BV250 thin film being of higher thickness, subsequently facilitating there being numerous active sites for target gas molecule diffusion.

Structural analysis

Fig. 2 depicts the powder X-ray diffraction spectra of $BiVO_4$ thin films deposited at various substrate temperatures. The prominent diffraction peaks are observed at 19.35° (1 0 1), 29.38° (1 1 2), 31.02° (0 0 4), 35.67° (2 0 0), 40.36° (2 1 1), 42.91° (1 0 5), 46.35° (1 2 3), 47.70° (2 0 4), 50.70° (2 2 0), 53.72° (3 0 1), 56.44° (1 2 5), 58.99° (1 0 7), 59.74° (3 1 2), and 60.41° (2 2 4), which is in accordance with ICDD card no: 01-075-2481, and firmly ratifies the formation of a tetragonal scheelite $BiVO_4$ structure with the space group $I4_1/a$. Notably, among all of the prepared films (BV150, BV200, BV250), no discernible secondary peaks were observed in the XRD pattern and the peaks exhibit strong intensity and are comparatively sharp, which confirms the high crystallinity of the tetragonal scheelite $BiVO_4$ thin films.[27,28]

The observed powder X-ray pattern reveals that the (112) plane is prominent when the substrate temperature is varied over 150 °C to 250 °C. This discloses that the crystallinity of the deposited films increases with respect to a rise in substrate temperature. With the help of the major peaks, the cell volume (V), lattice constant ($a = b \neq c$), crystallite size (D), microstrain (ε), and dislocation density (δ) were calculated and the results are tabulated in Table 1.

The lattice parameters and cell volume linearly decreased with respect to the rise in growth temperature. Similarly, the average crystallite size (D) also increased with an increase in the substrate temperature, which is attributed to the aggregation of neighbouring tiny crystals in the system into larger ones.

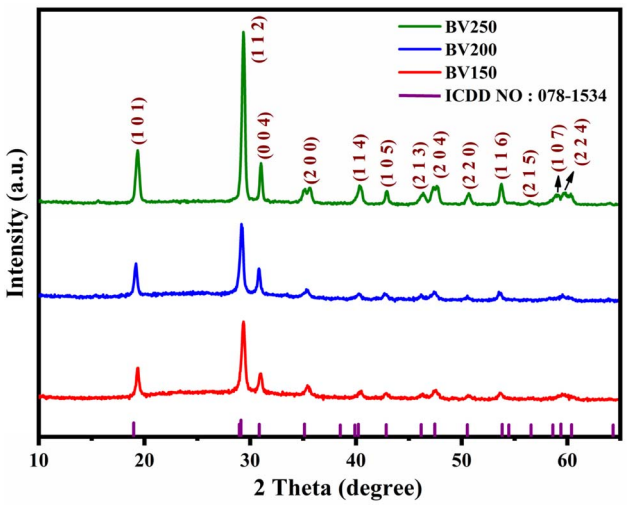

Fig. 2 The substrate temperature-dependent diffraction patterns of the $BiVO_4$ thin films.

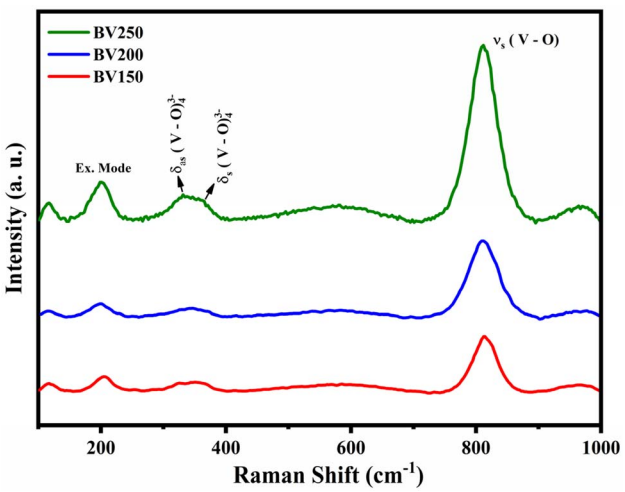

Fig. 3 The vibrational modes of substrate temperature-varied $BiVO_4$ thin films.

Table 1 The XRD findings from the substrate temperature-varied $BiVO_4$ thin films

Sample	Lattice constant ($a = b$)	Lattice constant (c)	Cell volume (a^3)	Average crystallite size (D)	Micro strain (ε) $\times 10^{-3}$ (line^{-2} m^{-4})	Dislocation density (δ) $\times 10^{15}$ (nm^{-2})
BV150	5.1100	11.5996	302.88	25.44	4.3632	15.4477
BV200	5.0698	11.5864	297.80	30.68	4.2406	10.6192
BV250	5.0466	11.5256	293.53	31.04	4.1897	10.3726

$$V = a^3 \quad (1)$$

$$D = (0.9 \times \lambda)/(\beta \cos \theta) \quad (2)$$

$$\delta = 1/D^2 \quad (3)$$

$$\varepsilon = \frac{\beta}{4 \tan \theta} \quad (4)$$

Dislocation density is a line defect, and is known as the number of lattice dislocations (mismatches) per unit area.[29] In our work, the dislocation density decreases with an increase in substrate temperature. Meanwhile, the microstrain indicates the lattice imperfection concentration, which also decreases with an increase in substrate temperature. This indicates that the film has a lower dislocated network and strain in the crystal lattice, which facilitates higher crystalline properties of the prepared thin films.

Raman spectroscopy

Raman spectroscopy is a valuable tool for unravelling the structural information, crystallization, and local structure of materials.[30] The growth temperature-controlled $BiVO_4$ thin films were excited using a green laser (532 nm), and the resulting spectra are depicted in Fig. 3. All of the deposited thin films exhibited Raman bands at around 118 cm^{-1}, 202 cm^{-1}, 329 cm^{-1}, 369 cm^{-1}, and 813 cm^{-1}, which correspond to the vibrational modes of $BiVO_4$. The Raman vibrational bands at 118 and 201 cm^{-1} are ascribed to the translational and rotational modes (external mode) of $BiVO_4$. Meanwhile, the vibrational modes centred at 329 cm^{-1} and 369 cm^{-1} validate the asymmetric (υ_{as}) and symmetric (υ_s) vibrations of the (V–O) group, respectively. The prominent band centred at 813 cm^{-1} denotes the (V–O) stretching mode υ_s vibration, along with a minor peak at around 710 cm^{-1} representing the υ_{as} (V–O) vibrational mode.[31–33] All of these vibrational bands collectively confirm the successful formation of $BiVO_4$ thin films.

UV-vis spectroscopy

UV-visible spectroscopy was employed to measure the absorbance spectra of the $BiVO_4$ thin films and the resultant trace is depicted in Fig. 4a. When the substrate temperature increases, the absorbance edge is shifted to a higher wavelength (red shift) due to thermally induced defects.[15] The quantitative estimations on the bandgap energies of the substrate temperature-varied $BiVO_4$ thin films were determined from the absorbance spectra through the Tauc plot method (eqn (5)), depicted in Fig. 4b.

$$(\alpha h\upsilon)^m = A(h\upsilon - E_g) \quad (5)$$

where E_g is the bandgap energy, $h\upsilon$ is the photon energy, A is a constant, and m is the allowed direct transition, which is equal to 2.

The calculated bandgap energy (E_g) values are 2.48, 2.38, and 2.24 eV for BV150, BV200, and BV250, respectively. At higher growth temperatures, the internal compressive stress is released, which causes an expansion in the crystal lattice, which in turn decreases the bandgap energy of the deposited films.[34–36] Hence, a thin film sensor with a reduced bandgap facilitates enhanced gas sensing performance.

Atomic force microscopy

Atomic force microscopy is a precise characterization technique at the nanoscale level, which offers a quantitative assessment of surface irregularities such as surface roughness (Ra), root mean square roughness (Rq), skewness (Ssk), the existence of peaks and valleys (kurtosis (Sku)), *etc.*[37,38] In this work, surface topological images were measured in contact mode with dimensions of 10 × 10 μm, as depicted in Fig. 5a–f. The surface temperature-varied chemically sprayed $BiVO_4$ thin films were shown to be crack-free, densely packed thin films with significant surface irregularity. Similarly, the spray-deposited BV150 and BV200 thin film sensors exhibited surface irregularities, including peaks and valleys, in their 2D and 3D topographical images. At higher growth temperatures, aerosols are completely evaporated and their residues reach random sites in the substrate; as a result, abrupt nucleation takes place over random sites. This is attributed to achieving higher surface roughness on the film.[39] In the same way, the chemically sprayed BV250 thin film sensor also showed increased roughness with an interconnected fibrous

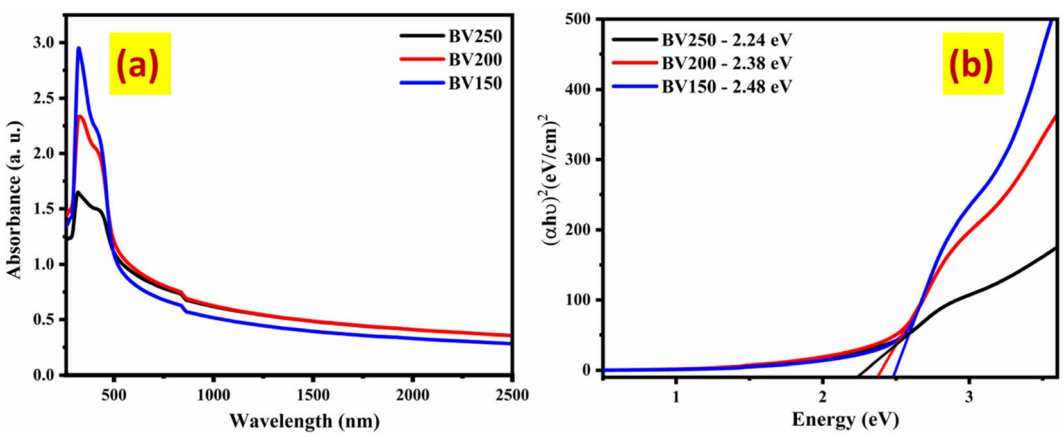

Fig. 4 (a) The absorbance spectra and (b) the Tauc plots for the substrate temperature-varied $BiVO_4$ thin films.

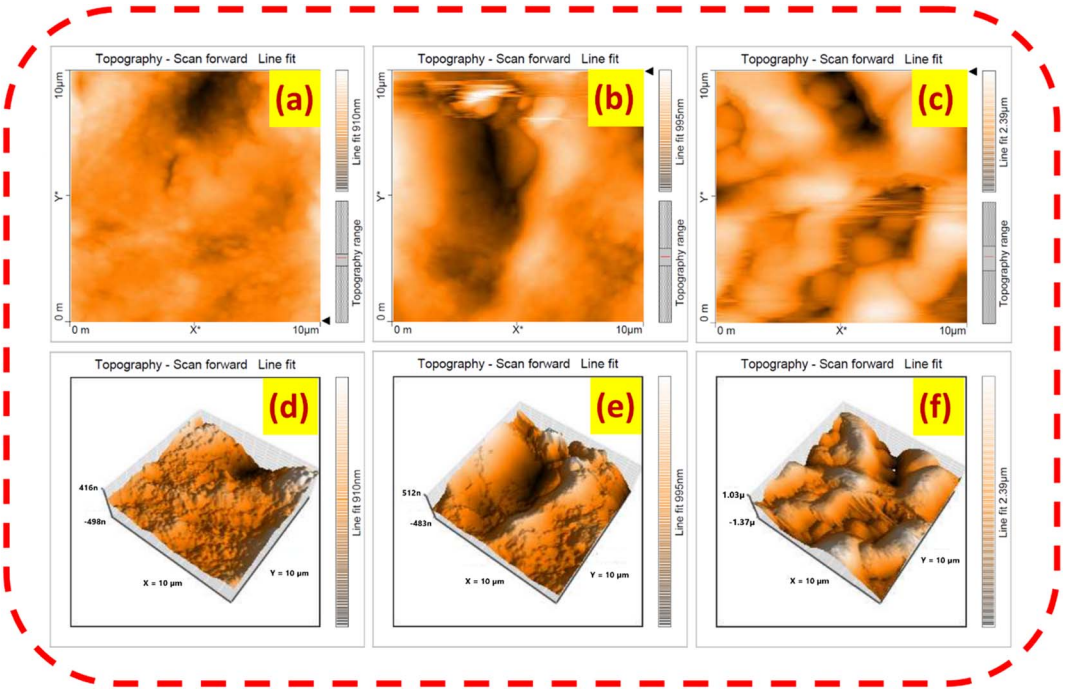

Fig. 5 (a, c and e) and (b, d and f) 2D and 3D topographical images of the substrate temperature-varied $BiVO_4$ thin films.

network. The average (Ra) and root mean square roughness (Rq) values are 93.48, 146.01, 375.73 nm and 132.28, 182.43, 450.91 nm for the BV150, BV200 and BV250 thin films, respectively. In addition, the skewness gives information about the asymmetric distribution profile; meanwhile, kurtosis gives details of the height (tail) profile of the specified area.[40,41] The BV150, BV200, and BV250 thin films sensor's skewness and kurtosis values are 0.4797, 0.3365, 0.3011 nm and 2.5420, 2.6630, 2.7040 nm, respectively. The skewness profile with a positive value shows a right angle flattened spatial pattern, along with increased kurtosis values disclosing longer tails at the sensor surface.[40,41] The BV250 thin film sensor illustrates the highest average surface roughness, increased kurtosis and lower skewness value compared to the other films (as shown in Table 2), suggesting a larger surface area, which increases the percolation pathway to ionized oxygen species and the target gas molecule interaction. These are the crucial factors accountable for the BV250 thin film sensor achieving a higher sensor response towards the target gas molecules.[42,43]

Contact angle measurement

Contact angle measurement stands as an extensive technique for delving into the wetting properties of the desired material. A contact angle value of less than 90° indicates a hydrophilic nature, while a value exceeding 90° indicates a hydrophobic nature.[44] The substrate temperature varied BV150, BV200 and BV250 thin film sensor contact angle values are depicted in

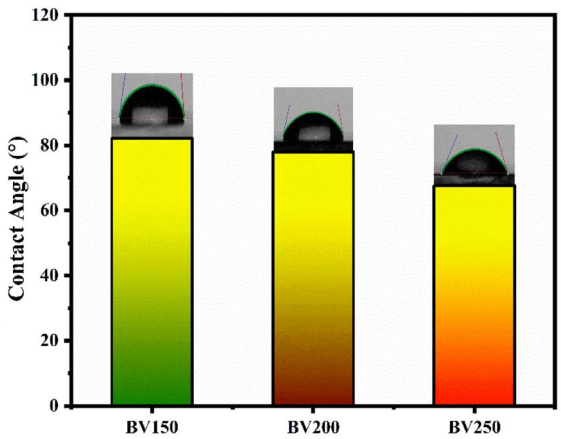

Fig. 6 The water contact angle of the substrate temperature-varied $BiVO_4$ thin films.

Table 2 The band gap, average roughness, RMS roughness, skewness, kurtosis and contact angle of the BV150, BV200 and BV250 thin films

Thin film sensor	Film thickness (nm)	Bandgap (eV)	Average roughness (Sa) (nm)	RMS roughness (Sq) (nm)	Skewness (Ssk) (nm)	Kurtosis (Sku) (nm)	Contact angle (°)
BV150	695	2.48	93.48	132.08	0.4797	2.5420	82.11
BV200	765	2.38	146.01	182.43	0.3365	2.6630	77.95
BV250	895	2.24	350.08	428.86	0.3011	2.7040	67.52

Fig. 6. The contact angle measurement values of the BV150, BV200 and BV250 thin films are 82.11°, 77.95°, and 67.52°, respectively. In this case, all three deposited $BiVO_4$ thin film values are less than 90°, which confirms their hydrophilic nature. Among all the films, the BV250 film shows a good hydrophilic nature (67.52°) (shown in Table 2), which possibly enhances the target adsorption rate at the sensor surface.[44,45]

Scanning electron microscopy

The morphology of the prepared BV150, BV200, and BV250 thin films was analysed using a scanning electron microscope, as shown in Fig. 7. The surface morphology of the $BiVO_4$ thin film deposited on a soda lime glass substrate at 150 °C (BV150) shows a slightly homogenous irregular nanograin morphology over the covered area (shown in Fig. 7a and b). It is observed that the average size of the irregular nanograins is about 168 ± 33 nm. When the substrate temperature increased to 200 °C (BV200), an agglomerated cluster-like morphology was observed due to the aggregation of the irregular nanograins with fewer macro-pores (as shown in Fig. 7d and e). Furthermore, a rise in substrate temperature to 250 °C (BV250) results in an interconnected fibrous network with augmented macropores, which is consistent with the AFM analysis shown in Fig. 7(g and h). This structure facilitates enhanced percolation pathways for the target gas molecule's diffusion compared to other films. The EDAX spectrum and colour mapping analysis were acquired for the substrate temperature-varied $BiVO_4$ films, to disclose the elemental composition of Bi, V, and O, which is depicted in Fig. 7(c, f, i) and 8(a–l). The even distribution of the Bi, V and O elements throughout the film is confirmed through this analysis. All three thin films showed significant weight and atomic percentages in the EDAX spectrum (Fig. 7(c, f and i)), which is influenced by the growth (substrate) temperature. In addition, elemental colour mapping analysis also shows that there is a significant drop in oxygen content on increasing the substrate temperature, which is also consistent with the EDAX spectrum. The existence of a low oxygen content in the deposited film (BV250) may lead to oxygen deficiencies or vacancies,[10,46] which can exponentially alter the material's physiochemical properties. The enhanced oxygen vacancies can act as trapping sites for ionized oxygen species adsorption and target gas molecule diffusion on the sensor material. Similarly, the BV250 thin film sensor has a lower oxygen content, which may favour the formation of larger oxygen vacancies than on the other films, which leads to a higher sensor response.

X-ray photoelectron spectroscopy

The surface elemental composition and the possible chemical states of the $BiVO_4$ thin films were acquired using X-ray photoelectron spectroscopy. The presence of Bi, V and O elements in all three thin films ratifies the successful formation of the substrate temperature-varied (BV150, BV200, BV250) thin films, as shown in Fig. 9(a) and 1(a–f) in the ESI.† Fig. 9(b) shows the BV250 film's two characteristic peaks located at 158.57 and 163.86 eV belonging to Bi $4f_{7/2}$ and Bi $4f_{5/2}$, respectively. The spin–orbit splitting value for these peaks is 5.3 eV, which aligns with the Bi^{3+} cationic element.[32] Similarly, the peaks at 516.24 and 523.60 eV correspond to V $2p_{3/2}$ and V $2p_{1/}$

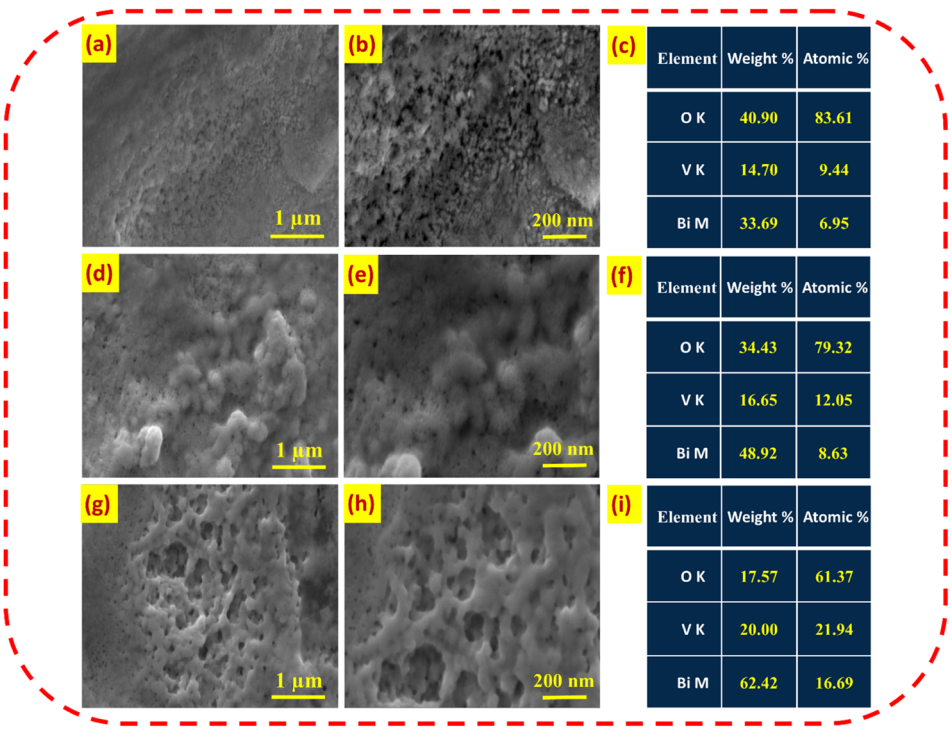

Fig. 7 The scanning electron microscopy images of $BiVO_4$ thin films (a, b, d, e, g and h) and (c, f and i) EDAX weight and atomic percentages of the substrate temperature-varied $BiVO_4$ thin films.

$_2$, which are the characteristic peaks of the V^{5+} cationic element, as shown in Fig. 9(d).[32,33] Fig. 9(c) shows the deconvoluted peak fitting of the O 1s spectrum, which is overlapped into three characteristic peaks. The peak around 529.31 eV is considered as lattice oxygen; meanwhile, the peaks located at 530.69 eV and 532.17 eV are defective vacancies and hydroxide ions, respectively.[47–50] The defective oxygen percentage of the BV250 film is about 16%, whereas for the BV200 and BV150 thin films, the percentages are 8.71 and 7.78%, respectively. This implies that the BV250 film has a larger amount of defective oxygen than the BV200 and BV150 films, which provides numerous active sites (acting as vacancy sites) for the adsorbed oxygen. This helps to achieve a higher sensor response to the target gas.

Gas sensing performance

The chemi-resistive gas sensing attributes of the BV150, BV200 and BV250 thin film sensors were scrutinized for their potential application in the detection of volatile organic liquids (VOCs). The selected VOCs were chosen based on their relevance to both industrial and environmental applications. Specifically, amine groups were chosen due to their widespread use in laboratories and industry, and their potential health hazards. Exposure to these gases can cause depression of the central nervous system, irritation of the eyes, nose and throat, and in the case of long-term exposure can be lethal. The safety limit concentrations for ammonia and dimethylamine are 25 ppm and 10 ppm for 8 and 10 h, respectively. To ensure workplace safety, the detection of ammonia is also crucial. Therefore, there is a strong demand for sensor materials that exhibit high sensitivity and selectivity towards ammonia, good stability, simplicity, and low cost. Similarly, the spray-deposited tetragonal scheelite-structured $BiVO_4$ thin film sensors should completely recover back to the initial baseline current after exposure to ammonia gas.

Selectivity is a specific criterion for a gas sensor to determine its ability to detect a particular gas among various interfering gases. Poor selectivity can limit the sensing performance, as it potentially leads to cross-selectivity in room temperature scenarios. The baseline current value of the deposited tetragonal scheelite-structured $BiVO_4$ thin films was about 4.67×10^{-10}, 4.60×10^{-10} and 4.52×10^{-10} for the BV150, BV200 and BV250 thin film sensors, respectively. The sensor response of the desired thin film sensor can be defined as the ratio between the baseline current in the gas (I_{gas}) divided by the baseline current in air (I_{gas}). The volatile organic compound sensing responsiveness can be witnessed through the selectivity test, which is depicted in Fig. 10(a). In our study, the BV250 thin film was tested against a 75 ppm concentration of ethanol (C_2H_5OH), acetone ($(CH_3)_2CO$), 2-propanol ($(CH_3)_2CHOH$), ammonia (NH_3), dimethylamine ($(CH_3CH_2)_2NH$), and trimethylamine ($N(CH_2CH_3)_3$), and the resultant sensor responses ($S = I_{gas}/I_{air}$) are 2.66, 1.28, 6.66, 900, 15.95, and 18.24, respectively. This observation reveals that the BV250 film is highly selective towards ammonia gas. The reason for achieving the highest sensor response to ammonia gas is ascribed below. (i) NH_3 molecules are smaller (in size) than other target gases, which can easily permeate between the interconnected fibrous network morphology. This suggests more ammonia vapour diffusion and the release of a free electron. (ii) NH_3 molecules readily donate more electrons to the vanadium site (V=O) at room temperature. (iii) The existence of lone pair electrons in ammonia gas enhances the interaction with the BV250 thin film sensor, which improves the overall sensor response to ammonia vapour. (iv) In comparison with the BV150 and BV200 thin films, the interconnected fibrous morphology of the BV250 film facilitates more shelter to ammonia vapour, which induces more oxygen molecule adsorption.[51,52] All these cumulative factors form a possible rationale for the BV250 thin film sensor's higher sensor response and selectivity towards ammonia vapour.

The transient response curves of the BV150, BV200, and BV250 thin film sensors were assessed for ammonia gas vapour at different concentrations from 25 to 150 ppm at room temperature, as depicted in Fig. 10(b), 3 and 4 in the ESI.† The irregular nanograin BV150 film's exhibited sensor response was about $S = I_{gas}/I_{air} = 634$ for 150 ppm at room temperature (RT). Similarly, the BV200 film with an aggregated cluster-like morphology (with macropores) exhibited a sensor response $S = I_{gas}/I_{air} = 658$ for 150 ppm at RT. The interconnected fibrous network morphology (with augmented macropores) meant that the BV250 film's exhibited sensor response was about $S = I_{gas}/I_{air} = 1621$ for 150 ppm at RT. Comparatively, the BV250 thin film sensor's sensor response was enhanced by 1.2 and 2.1-fold-times compared to BV200 and BV150 films for 150 ppm at room temperature, respectively. This may be attributed to the availability of the interconnected fibrous network morphology, which potentially enhances the large reactive surface area, offering numerous active sites for ammonia vapour's adsorption and diffusion and facilitating the redox reaction. In addition to that, a higher film thickness, reduced bandgap and increased surface roughness pave the way to more ammonia vapour diffusion on the sensor surface, which aids in achieving the highest sensor response. The transient responsive traces exhibit a consistent upward trend in terms of sensor response with respect to an increase in ammonia concentration, which indicates good linearity of the gas sensors (shown in Fig. 10(d)). As a result, the BV250 film achieved the highest sensor response to ammonia vapour compared to the other films.

A minimum criterion for an ideal sensing layer is that after exposure to the target gas, the material should return to its initial baseline current value. When assessing the real-time efficacy of the chemi-resistive gas sensor, response time and recovery time are crucial parameters. Fig. 10(c) shows the BV250 thin film's response and recovery time trend *versus* ammonia concentration. The response time of the sensor is defined as 90% of the elapsed time taken to reach a steady-state current signal after the gas purge; meanwhile, the recovery time is the duration for the steady-state current signal to revert back to its initial baseline current after the removal of the purged gas in the chamber. The substrate temperature-varied BV150, BV200, and BV250 film's response and recovery times were 130 s, 180 s, 190 s and 10 s, 13 s, and 16 s for 25 ppm of NH_3 at room temperature, respectively. The BV250 thin film showed an excellent sensor response, and a reasonable response time and

recovery time, which makes it a potential candidate for ammonia detection at room temperature (as shown in Fig. 2 in the ESI†). During the practical usage of chemi-resistive gas sensors, both repeatability and stability are very crucial. The ability to reproduce a consistent sensor response across multiple cycles is known as repeatability. Fig. 10(e) shows a BV250 thin film sensor's repeatability plot for 25 ppm concentration of ammonia at room temperature. The fabricated sensor successfully maintained a stable sensor response (I_{gas}/I_{air} = 58.82 for 25 ppm) over 4 cycles at room temperature. Stability tests were performed to evaluate the long-term performance of the BV250 thin film, which was carried out after a period of one-week intervals. Meanwhile, the fabricated sensor is stored in a desiccator and kept in a dry place. The BV250 thin film sensor maintained a consistent sensor response (I_{gas}/I_{air} = 58.20 for 25 ppm) with little variation over the lifespan of 50 days (as shown in Fig. 10(f)), which effectively shows prolonged ammonia detection at room temperature.

To explore the moisture-resisting capabilities of the BV250 thin film sensor, various levels of relative humidity (11–75%) were employed using saturated salt solutions. To maintain a consistent humidity environment in the test chamber, lithium chloride (11%), magnesium chloride (32%), magnesium nitrate (52%) and sodium chloride (75%) were utilized. Assessment of the BV250 thin film sensor's performance across various humidity levels was performed for 25 ppm of NH_3 at room temperature. Initially, the baseline current of the BV250 film at ambient humidity was about 4.5×10^{-10}, as shown in Fig. 11(a). When the moisture level increased (11% to 75%), the thin film sensor's baseline current also increased. This is mainly attributed to the formation of a proton layer from surface-adsorbed (H_2O) water molecules.[1,9] The BV250 thin film sensor's sensor response was initially increased and then declined as the humidity level rose (as shown in Fig. 11(b)), which might be attributed to water molecules acting as a raw substance for the catalytic production of functional groups (HCOO– and –COO–) as redox reaction by-products.[53,54] However, a rise in humidity gradually decreases the sensor response of ammonia adsorption caused by the swift competitive adsorption of water molecules.

NH_3 sensing mechanism

A chemi-resistive metal oxide thin film gas sensor shows a swift signal when exposed to target gases. Commonly, the redox reaction followed by charge transfer governs the chemi-resistive gas sensing mechanism.[48,55–58] When an n-type semiconductor is exposed to the ambient air, oxygen molecules (O_2^-, O^-, and O^{2-}) are trapped over the sensor surface based on their operating temperature conditions; consequently, the metal oxide semiconductor resistance is increased. If the operating temperature is <100 °C (eqn (7)), between 100 °C and 300 °C (eqn (8)) or above 300 °C (eqn (9)), the available oxygen species for the reaction are O_2, O_2^- and O^-, respectively (as shown in eqn (6)–(9)). These oxygen species are adsorbed on the sensor surface and transformed into O_2^-, O^- and O^{2-} (ionized form) correspondingly.[11,59]

$$O_2(gas) \rightarrow O_2(ads) \quad (6)$$

$$O_2(ads) + e^-(\text{from sensor surface}) \rightarrow O_2^-(ads) \quad (7)$$

$$O_2^-(ads) + e^-(\text{from sensor surface}) \rightarrow 2O^-(ads) \quad (8)$$

$$O^-(ads) + e^-(\text{from sensor surface}) \rightarrow O^{2-}(ads) \quad (9)$$

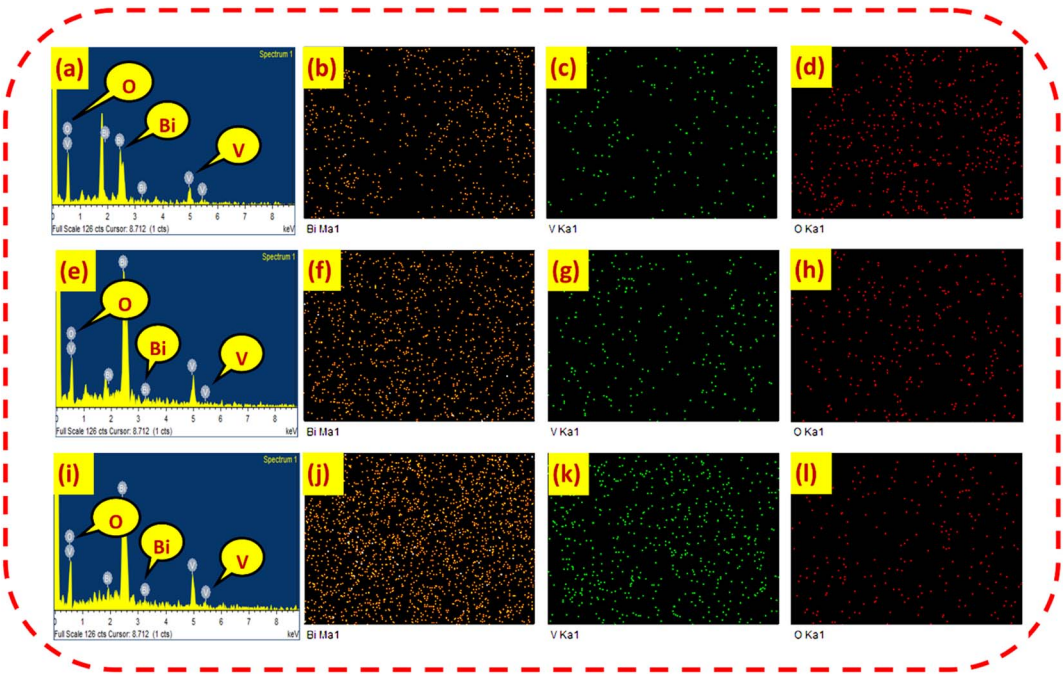

Fig. 8 (a–d), (e–h), and (i–l) The EDAX spectrum and elemental colour mapping of the BV150, BV200, and BV250 films, respectively.

$$NH_3(gas) \rightarrow NH_3(ads) \quad (10)$$

$$4NH_{3(ads)} + O_{2(ads)}^{-} \rightarrow 2N_2 + 6H_2O + 3e^{-} \quad (11)$$

During gas sensing analysis, the thin film sensor is exposed to clean air to ensure a stable baseline current or resistance. A room temperature sensing suggests that the oxygen ions involved in the chemisorption process are predominantly O_2^- ions. These ions adsorb onto the $BiVO_4$ thin film, thereby extracting the electrons from its conduction band and localizing them on the sensor surface. The diminution of electron density in the core facilitates electron depletion layer formation on the surface of the metal oxide semiconductor. Consequently, upward band bending and the establishment of a potential barrier occurs. Thereafter, the target gas was introduced into the gas sensing chamber. The rapid exposure of NH_3 gas molecules to the thin film sensor surface initiates a redox reaction at the surface of the metal oxide semiconductor. This reaction enables the transfer of electrons, thus resulting in a change in the baseline current of the sensing layer. Similarly, the NH_3 gas molecules are capable of capturing negatively charged oxygen adsorbates, and thereby free electrons are released, which are sent back to the conduction band of $BiVO_4$, concurrently producing N_2 and H_2O as byproducts (given in eqn (10) and (11)). In this case, an augmented amount of charge carriers was released, which diminishes the electron depletion layer and potential barrier of the metal oxide semiconductor. This resulted in a decrease in the baseline resistance of the thin film sensor in an ammonia environment. After the evacuation of the target gas from the sensing chamber, outer air is purged to interact with the sensing layer. This interaction increases the electron depletion layer and potential barrier due to the re-adsorption of oxygen adsorbates on the sensing layer. The sensor response (S) was evaluated using eqn (12). The gas sensing performances of different substrate temperature-deposited tetragonal scheelite-structured $BiVO_4$ thin films are shown in Fig. 12.

$$S = \frac{I_{gas}}{I_{air}} \quad (12)$$

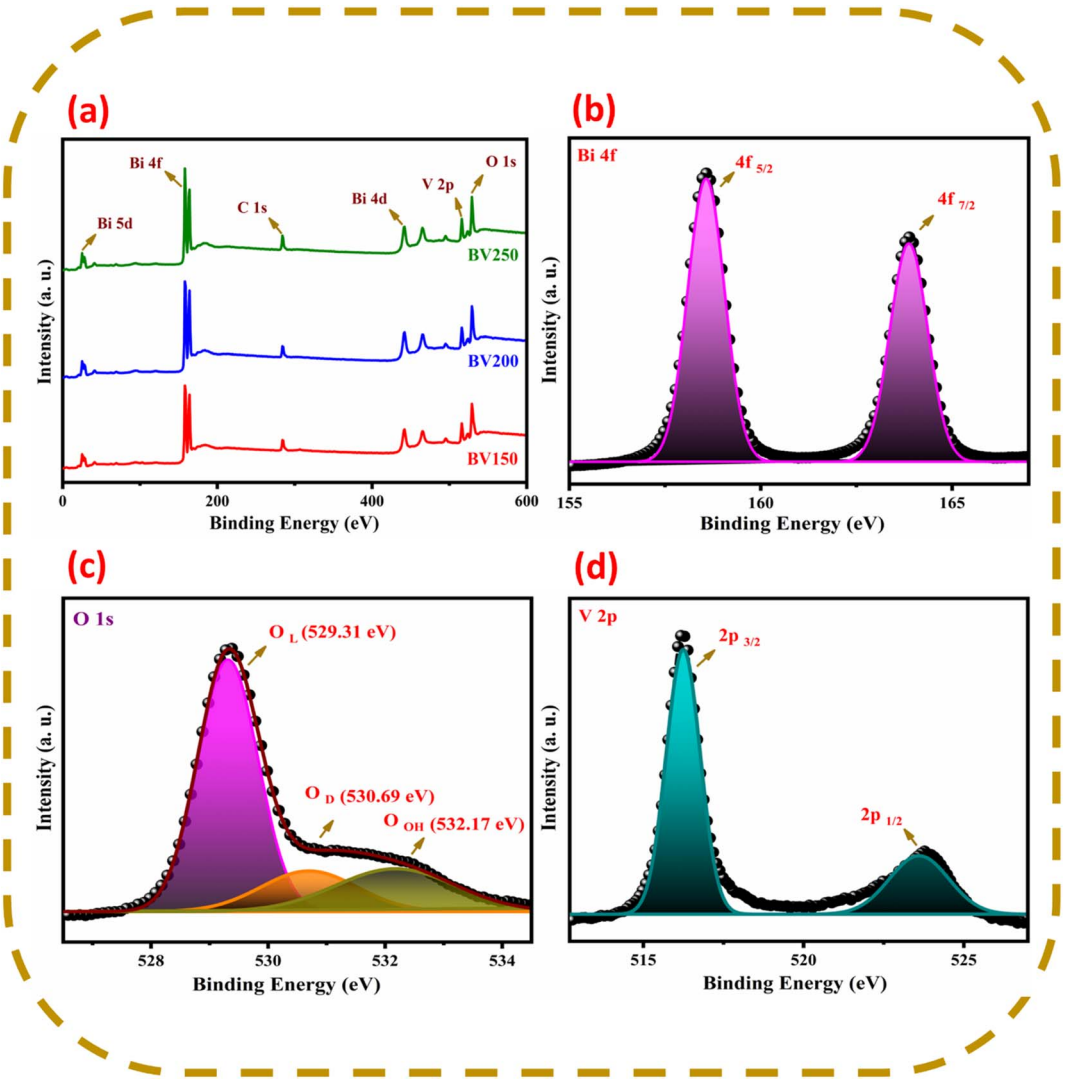

Fig. 9 (a) The survey spectrum of the BV150, BV200 and BV250 thin films. (b–d) The high-resolution spectra of Bi 4f, O 1s and V 2p, respectively.

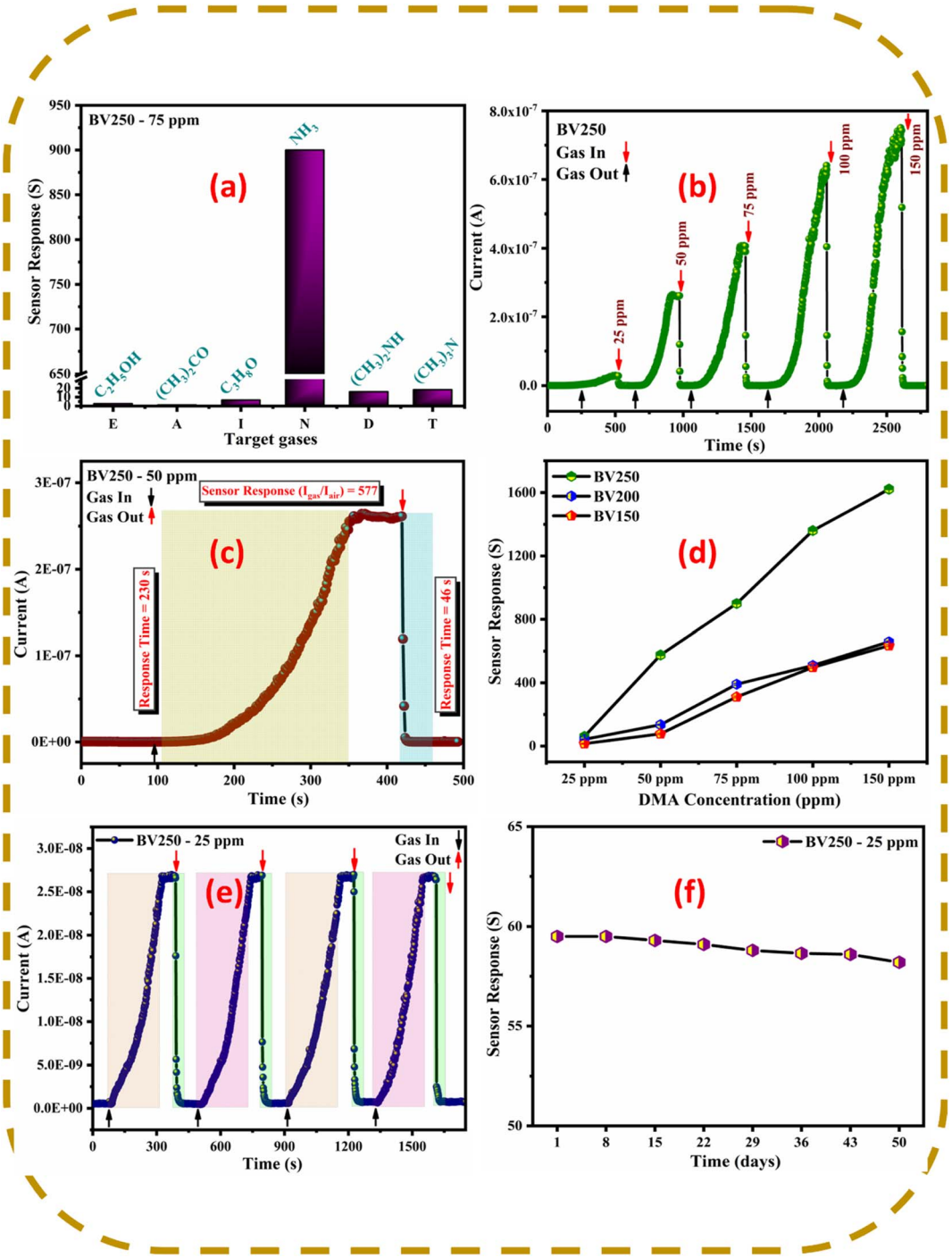

Fig. 10 (a) Selectivity plot, (b) transient responsive curve, (c) sensor response, response and recovery times, (d) substrate temperature of deposited $BiVO_4$ films *vs.* sensor response, (e) repeatability and (f) stability plot disclosing the gas sensing performance of the BV250 film at room temperature.

I_{gas} = current value in gas, I_{air} = current value in air.

It was found that the sensor response was influenced by the thickness of the $BiVO_4$ film.[10,60,61] Basically, a film with higher thickness provides a larger space for the percolation of adsorbed oxygen species and target gases, which leads to a higher sensor response being achieved.[10,25,62,63] Our scrutinization discloses that the calculated thickness was about 695 ± 0.021 nm, 765 ± 0.007 nm, and 895 ± 0.007 nm for the BV150, BV200 and BV250 thin films, respectively. As mentioned earlier, the BV250 thin film sensor with higher thickness (895 nm) showed an enhancement in the sensor response towards ammonia gas compared to other (lower thickness) thin film sensors. The BV250 thin film sensor demonstrated superior ammonia gas sensing performance compared to the other films

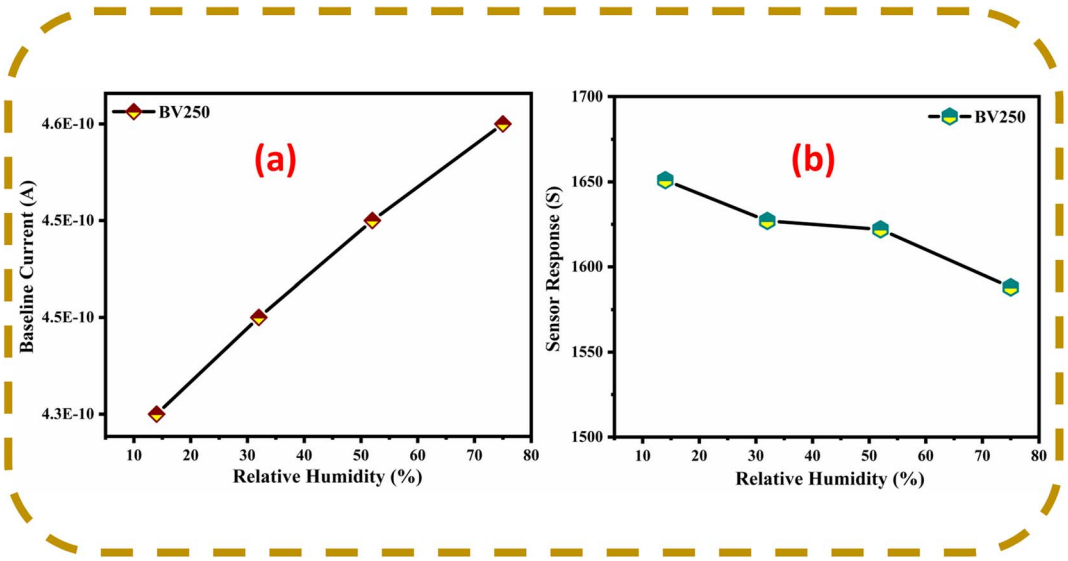

Fig. 11 The moisture resisting performance: (a) relative humidity *vs.* baseline current and (b) relative humidity *vs.* sensor response of the BV250 film.

due to its unique interconnected fibrous morphology. This structure facilitates a larger percolation path to ionized oxygen species adsorption and the target gas molecule diffusion for redox on the sensing material. Additionally, the larger grain boundaries within the BV250 film offer an efficient electron transfer channel during gas interaction, further leading to a higher sensor response. These combined factors contribute to the enhanced sensor response and selectivity of the BV250 sensor towards ammonia gas at room temperature. In contrast, a thin film sensor with a lower thickness (BV150 and BV200) displayed lower sensing performance due to the irregular nanograins and agglomerated cluster-like structures, and the reduced grain boundaries restricted the target gas (NH_3) adsorption. Similarly, the BV250 thin-film sensor has a reduced bandgap compared to other films, which lowers the activation energy, thereby increasing the intrinsic carrier concentration.[10,64,65] The higher population of charge carriers (*i.e.*, electrons) within the material favours enhanced surface reactivity through ionized oxygen adsorbates. This enables rapid gas molecule diffusion on the sensor surface, resulting in a higher sensor response being achieved. Morphological assessment using SEM demonstrates that the BV250 thin film sensor possesses an interconnected fibrous network with an augmented macropore. This nanostructure offers a high surface-to-volume ratio, which enhances the availability of active sites for the ionized oxygen species adsorption and target

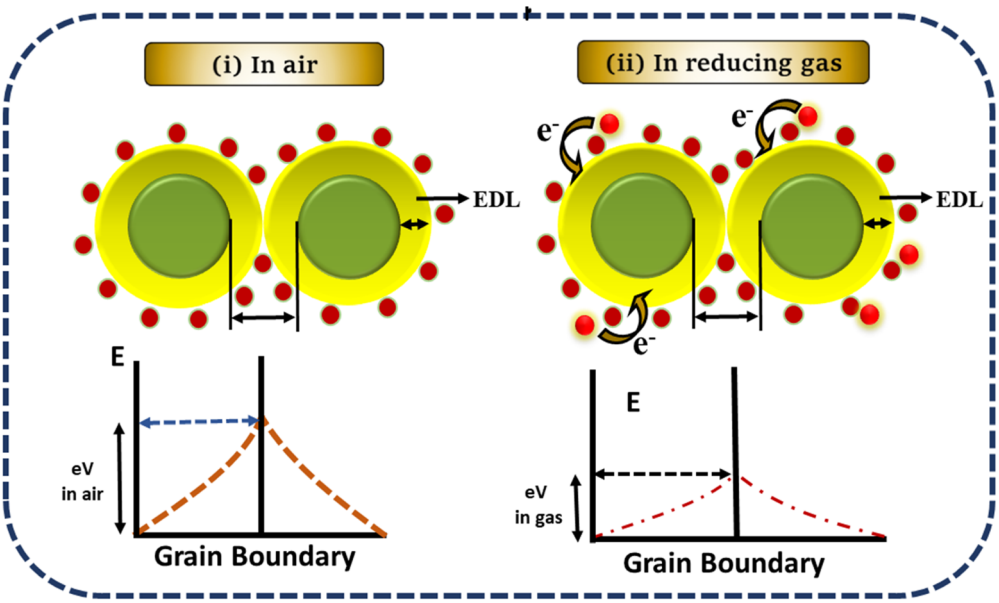

Fig. 12 Chemi-resistive gas sensing mechanism.

gas molecule diffusion compared to other films. In addition to that, the BV250 thin film sensor has an increased surface roughness, higher kurtosis and lower skewness values affording larger spikes to the thin film sensor surface. Also, the BV250 thin film sensor exhibited a hydrophilic nature, which ratifies swift ionized oxygen species adsorption and target gas molecule diffusion on the sensor surface. Moreover, the narrow scan O 1s spectra from XPS (Fig. 9) reveal the presence of defective oxygen (acting as vacancies), which is very crucial for the ammonia gas sensing performance. The percentages of defective oxygen are 16, 8.71 and 7.78% for BV250, BV200, and BV150, respectively. These results are highly consistent with elemental quantification (Fig. 7(c, f, i) and 8). This scrutiny also discloses that the BV250 thin film sensor's increased concentration of defective oxygen enables more ionized oxygen species adsorption and target gas molecule diffusion on the sensor surface. It is noteworthy to mention that the synergetic effects of the BV250 thin film sensor's higher thickness (895 nm), reduced bandgap (2.24 eV), increased surface roughness (350.08 nm), higher defective oxygen content (16%), hydrophilic nature (67.52°), and unique inter-connected fibrous network morphology with augmented macropores are accountable for the enhanced ionized oxygen species adsorption and the target gas molecule diffusion on the sensor surface compared to other films. All these cumulative reasons are responsible for the BV250 thin film sensor achieving an ultra-high sensor response, and good response and recovery times compared to other thin film sensors. The same film exhibits high stability and repeatability, and is also well-suited for room temperature detection of ammonia gas.

Conclusion

Growth temperature-varied tetragonal scheelite-structured $BiVO_4$ thin films were successfully deposited through the chemical spray pyrolysis technique. All of the films were subjected to the necessary characterization to study their physiochemical properties and finally a gas sensing study was employed to analyse their sensing capability. The BV250 film showed an ultra-high sensor response (I_{gas}/I_{air} = 900 at 75 ppm) towards ammonia vapour compared to the other films even at room temperature. The gas sensing measurement of the BV250 film firmly discloses its stability (I_{gas}/I_{air} = 58.2 for 25 ppm after the 50th day), good repeatability (up to 4 cycles) and moisture-resistance. The higher sensor response was attributed to the interconnected fibrous morphology, reduced bandgap (2.24 eV), higher roughness (350.08 nm), enhanced oxygen vacancies (16%) and hydrophilic nature (67.52°) of the BV250 film, endorsing it as a potential candidate to sense NH_3 at room temperature.

Data availability

Data will be made available on request.

Conflicts of interest

There are no conflicts to declare.

Acknowledgements

The authors would like to acknowledge VIT management for the facilities provided for this work. The authors would also like to convey their gratitude to all the lab members. The author Nallakumar Santhosh would like to thank Mr Darla Manohar, Mr Ravikumar Thangavel, and Ms Anju Thomas for their constant support.

References

1 S. Nallakumar and U. R. Muthurakku, *J. Hazard. Mater.*, 2024, 134041, DOI: **10.1016/j.jhazmat.2024.134041**.
2 M. Asim Safi and M. Shah, *Mater. Sci. Eng. B*, 2024, 116999, DOI: **10.1016/j.mseb.2023.116999**.
3 K. Sivaperuman, A. Thomas, R. Thangavel, L. Thirumalaisamy, S. Palanivel, S. Pitchaimuthu, N. Ahsan and Y. Okada, *Prog. Mater. Sci.*, 2024, 101222, DOI: **10.1016/j.pmatsci.2023.101222**.
4 I. Banga, A. Paul, D. C. Poudyal, S. Muthukumar and S. Prasad, *Am. Chem. Soc.*, 2023, 3307–3319, DOI: **10.1021/acssensors.3c00959**.
5 X. Song, R. Hu, S. Xu, Z. Liu, J. Wang, Y. Shi, J. Xu, K. Chen and L. Yu, *ACS Appl. Mater. Interfaces*, 2021, **13**, 14377–14384.
6 R. S. Andre, L. A. Mercante, M. H. M. Facure, R. C. Sanfelice, L. Fugikawa-Santos, T. M. Swager and D. S. Correa, *ACS Sens.*, 2022, 2104–2131, DOI: **10.1021/acssensors.2c00639**.
7 T. Ravikumar, L. Thirumalaisamy, S. Madanagurusamy and K. Sivaperuman, *J. Alloys Compd.*, 2023, 170568, DOI: **10.1016/j.jallcom.2023.170568**.
8 M. Khatib and H. Haick, *ACS Nano*, 2021, 7080–7115, DOI: **10.1021/acsnano.1c10827**.
9 T. Ravikumar and K. Sivaperuman, *Mater. Today Chem.*, 2024, 102049, DOI: **10.1016/j.mtchem.2024.102049**.
10 A. Dey, *Mater. Sci. Eng. B*, 2018, **229**, 206–217.
11 R. Xavier and K. Sivaperuman, *Mater. Today Commun.*, 2024, 107831, DOI: **10.1016/j.mtcomm.2023.107831**.
12 P. Srinivasan and J. B. B. Rayappan, *Sens. Actuators, B*, 2021, 130759, DOI: **10.1016/j.snb.2021.130759**.
13 I. Sharma, K. N. Kumar and J. Choi, *Sens. Actuators, B*, 2023, 132899, DOI: **10.1016/j.snb.2022.132899**.
14 V. S. Bhati, M. Kumar and R. Banerjee, *R. Soc. Chem.*, 2021, **9**, 8776–8808, DOI: **10.1039/d1tc01857d**.
15 S. Nallakumar, L. Thirumalaisamy, S. Madhanagurusamy, S. Kalainathan and M. Usha Rani, *New J. Chem.*, 2023, **47**, 11110–11122.
16 D. Chen, Q. Wang, R. Wang and G. Shen, *R. Soc. Chem.*, 2015, **3**, 10158–10173, DOI: **10.1039/c4ta06923d**.
17 M. Shi, H. Yang, Z. Zhao, G. Ren and X. Meng, *Chem. Commun.*, 2023, **59**, 4274–4287.
18 X. Meng and Z. Zhang, *J. Mol. Catal. A: Chem.*, 2016, 533–549, DOI: **10.1016/j.molcata.2016.07.030**.
19 T. Yang and D. Xia, *J. Cryst. Growth*, 2009, **311**, 4505–4509.
20 N. Rashmi, M. Majid and S. Sivakumar, *Phys. Chem. Chem. Phys.*, 2023, **25**, 27595–27605.
21 J. Pellicer-Porres, D. Vázquez-Socorro, S. López-Moreno, A. Muñoz, P. Rodríguez-Hernández, D. Martínez-García,

S. N. Achary, A. J. E. Rettie and C. B. Mullins, *Phys. Rev. B*, 2018, 214109, DOI: 10.1103/PhysRevB.98.214109.
22 T. G. Vo, J. M. Chiu, C. Y. Chiang and Y. Tai, *Sol. Energy Mater. Sol. Cells*, 2017, **166**, 212–221.
23 T. Kansaard, K. N. Ishihara and W. Pecharapa, *Phys. Status Solidi A*, 2023, **220**, 2200447, DOI: 10.1002/pssa.202200447.
24 A. M. S. Arulanantham, S. Valanarasu, A. Kathalingam, M. Shkir and H. S. Kim, *Mater. Res. Express*, 2018, 026412, DOI: 10.1088/2053-1591/aaed1b.
25 R. Souissi, N. Bouguila, B. Bouricha, C. Vázquez-Vázquez, M. Bendahan and A. Labidi, *RSC Adv.*, 2020, **10**, 18841–18852.
26 A. Ouhaibi, N. Saoula, M. Ghamnia, M. A. Dahamni and L. Guerbous, *Cryst. Res. Technol.*, 2022, **57**, 2100224, DOI: 10.1002/crat.202100224.
27 Y. Li, X. Xiao and Z. Ye, *Ceram. Int.*, 2018, **44**, 7067–7076.
28 J. Huang, G. Tan, L. Zhang, H. Ren, A. Xia and C. Zhao, *Mater. Lett.*, 2014, **133**, 20–23.
29 S. A. J. Jassim, A. A. R. A. Zumaila and G. A. A. Al Waly, *Results Phys.*, 2013, **3**, 173–178.
30 P. Colomban and A. Slodczyk, *Opt. Mater.*, 2009, **31**, 1759–1763.
31 V. Arulazi and S. Kalainathan, *J. Mater. Sci.: Mater. Electron.*, 2024, **35**, 347, DOI: 10.1007/s10854-024-12088-4.
32 C. Li, X. Qiao, J. Jian, F. Feng, H. Wang and L. Jia, *Chem. Eng. J.*, 2019, 121924, DOI: 10.1016/j.cej.2019.121924.
33 Y. Geng, P. Zhang, N. Li and Z. Sun, *J. Alloys Compd.*, 2015, **651**, 744–748.
34 D. Pathinettam Padiyan, A. Marikani and K. R. Murali, *Mater. Chem. Phys.*, 2002, **78**, 51–58.
35 S. A. J. Jassim, A. A. R. A. Zumaila and G. A. A. Al Waly, *Results Phys.*, 2013, **3**, 173–178.
36 A. H. Omran Alkhayatt, I. A. D. Al-Hussainy and O. A. C. Al-Rikaby, *Adv. Phys. Theor. Appl.*, 2014, **34**, 1–7.
37 M. Ramzan, E. Ahmed, N. A. Niaz, A. M. Rana, A. S. Bhatti, N. R. Khalid and M. Y. Nadeem, *Superlattices Microstruct.*, 2015, **82**, 399–405.
38 A. Ghaderi, A. Shafiekhani, S. Solaymani, Ş. Ţălu, H. D. da Fonseca Filho, N. S. Ferreira, R. S. Matos, H. Zahrabi and L. Dejam, *Sci. Rep.*, 2022, **12**, 3, DOI: 10.1038/s41598-022-16347-4.
39 A. B. Workie, H. S. Ningsih and S. J. Shih, *J. Anal. Appl. Pyrol.*, 2023, 105915, DOI: 10.1016/j.jaap.2023.105915.
40 S. R. Sriram, S. R. Parne, N. Pothukanuri and D. R. Edla, *Appl. Surf. Sci. Adv.*, 2023, 100411, DOI: 10.1016/j.apsadv.2023.100411.
41 A. A. Mane, S. A. Nikam and A. V. Moholkar, *Mater. Chem. Phys.*, 2018, **216**, 294–304.
42 D. P. Nagmani, A. Tyagi, T. C. Jagadale, W. Prellier and D. K. Aswal, *Appl. Surf. Sci.*, 2023, 149281, DOI: 10.1016/j.apsusc.2021.149281.
43 M. Proença, M. S. Rodrigues, C. Moura, A. V. Machado, J. Borges and F. Vaz, *Sens. Actuators, B*, 2024, 134959, DOI: 10.1016/j.snb.2023.134959.
44 J. Fan, J. Gao, H. Lv, L. Jiang, F. Qin, Y. Fan, B. Sun, J. Wang, M. Ikram and K. Shi, *J. Mater. Chem. A*, 2022, **10**, 25714–25724.
45 S. M. Ingole, Y. H. Navale, D. K. Bandgar, V. B. Patil, S. T. Navale, F. J. Stadler, N. S. Ramgir, S. K. Gupta, D. K. Aswal and R. S. Mane, *J. Colloid Interface Sci.*, 2017, **493**, 162–170.
46 S. Meena, K. S. Anantharaju, S. Malini, A. Dey, L. Renuka, S. C. Prashantha and Y. S. Vidya, *Ceram. Int.*, 2021, **47**, 14723–14740.
47 W. Pan, X. Zhou, Q. Lin, J. Chen, L. Lu and S. Zhang, *J. Mater. Chem. C*, 2022, **10**, 3129–3138.
48 T. Ravikumar, L. Thirumalaisamy, S. Madanagurusamy and S. Kalainathan, *Phys. Chem. Chem. Phys.*, 2023, **25**, 32216–32233.
49 G. Yuan, H. Zhang, Y. Cheng, Y. Zhong, Q. Zhuo and X. Sun, *J. Mater. Chem. C*, 2021, **9**, 14278–14285.
50 S. Zhang, P. Song, Q. Wang and Y. Ding, *Sens. Actuators, B*, 2023, 133239, DOI: 10.1016/j.snb.2022.133239.
51 V. Mounasamy, G. K. Mani, D. Ponnusamy, K. Tsuchiya, A. K. Prasad and S. Madanagurusamy, *J. Mater. Chem. A*, 2018, **6**, 6402–6413.
52 Z. Guo, B. Wang, X. Wang, Y. Li, S. Gai, Y. Wu and X. Cheng, *RSC Adv.*, 2019, **9**, 37518–37525.
53 M. S. Choi, A. Mirzaei, H. G. Na, S. Kim, D. E. Kim, K. H. Lee, C. Jin and S. W. Choi, *Sens. Actuators, B*, 2021, **340**, 129984.
54 H. Y. Li, C. S. Lee, D. H. Kim and J. H. Lee, *ACS Appl. Mater. Interfaces*, 2018, **10**, 27858–27867.
55 T. Ravikumar and K. Sivaperuman, *Colloids Surf., A*, 2024, 133382, DOI: 10.1016/j.colsurfa.2024.133382.
56 A. Thomas, L. Thirumalaisamy, S. Madanagurusamy and K. Sivaperuman, *Sens. Actuators, B*, 2024, 135043, DOI: 10.1016/j.snb.2023.135043.
57 R. Xavier, L. Thirumalaisamy, S. Madhanagurusamy and K. Sivaperuman, *Ceram. Int.*, 2024, **50**, 969–976.
58 K. Sankarasubramanian, K. J. Babu, P. Soundarrajan, T. Logu, G. Gnanakumar, K. Ramamurthi, K. Sethuraman and S. M. Senthil Kumar, *Sens. Actuators, B*, 2019, **285**, 164–172.
59 K. Sankarasubramanian, P. Soundarrajan, T. Logu, K. Sethuraman and K. Ramamurthi, *New J. Chem.*, 2018, **42**, 1457–1466.
60 K. Sivaperuman, A. Thomas, R. Thangavel, L. Thirumalaisamy, S. Palanivel, S. Pitchaimuthu, N. Ahsan and Y. Okada, *Prog. Mater. Sci.*, 2024, **142**, 101222.
61 T. Ravikumar, L. Thirumalaisamy, S. Madanagurusamy and S. Kalainathan, *Phys. Chem. Chem. Phys.*, 2023, **25**, 32216–32233.
62 R. Godbole, V. P. Godbole, P. S. Alegaonkar and S. Bhagwat, *New J. Chem.*, 2017, **41**, 11807–11816.
63 S. Nallakumar and U. R. Muthurakku, *Surface. Interfac.*, 2024, 104666, DOI: 10.1016/j.surfin.2024.104666.
64 C. Zhang, G. Liu, X. Geng, K. Wu and M. Debliquy, *Sens. Actuators, A*, 2020, 112026, DOI: 10.1016/j.sna.2020.112026.
65 A. Kumar, R. Kumar, R. Singh, B. Prasad, D. Kumar and M. Kumar, *Arab. J. Sci. Eng.*, 2021, **46**, 617–630.